Dalton Transactions

Accepted Manuscript

ROYAL SOCIETY OF CHEMISTRY

www.rsc.org/dalton

Graphical Abstract for:

Redox and acid–base properties of asymmetric non-heme (hydr)oxo-bridged diiron complexes

Anna Jozwiuk,[a] Audrey L. Ingram,[a] Douglas R. Powell,[a] Boujemaa Moubaraki,[b] Nicholas F. Chilton,[b] Keith S. Murray[b] and Robert P. Houser*[c]

[a]Department of Chemistry & Biochemistry, University of Oklahoma, Norman, OK 73019, USA. [b]Chemistry Department, Monash University, Clayton, Victoria 3168 Australia. [c]Department of Chemistry & Biochemistry, University of Northern Colorado, Greeley, CO 80639, USA.

Fax: +1 970 351 2176; Tel: +1 970 351 2877; E-mail: robert.houser@unco.edu

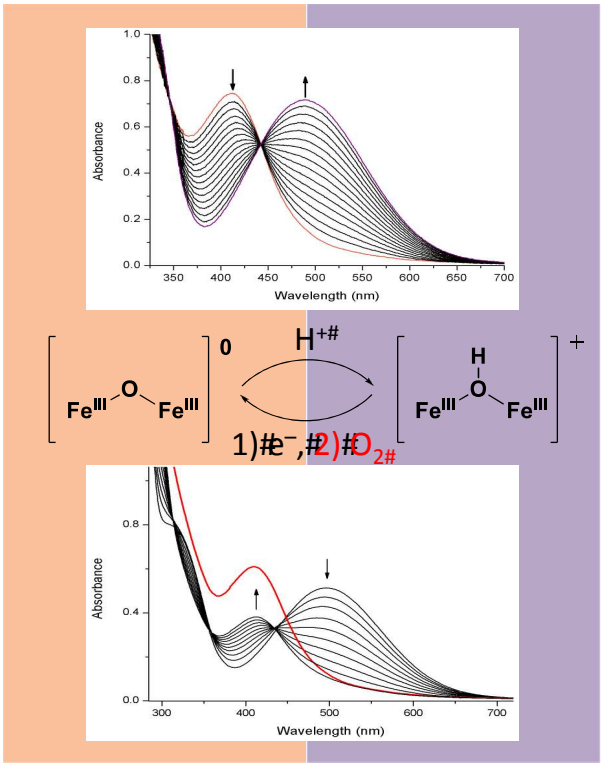

$[(FeL)_2(\mu\text{-}OH)]^+$, $[(FeL)_2(\mu\text{-}O)]$ and $[(FeL^{NO2})_2(\mu\text{-}OH)]^+$, were synthesized and characterized. Electrochemical and chemical reduction of $[(FeL)_2(\mu\text{-}OH)]BPh_4$ revealed disproportionation followed by proton transfer, and subsequent exposure to molecular oxygen results in the formation of $[(FeL)_2(\mu\text{-}O)]$.

Cite this: DOI: 10.1039/c0xx00000x

www.rsc.org/xxxxxx

ARTICLE TYPE

Redox and acid–base properties of asymmetric non-heme (hydr)oxo-bridged diiron complexes

Anna Jozwiuk,[a] Audrey L. Ingram,[a] Douglas R. Powell,[a] Boujemaa Moubaraki,[b] Nicholas F. Chilton,[b] Keith S. Murray[b] and Robert P. Houser*[c]

Received (in XXX, XXX) Xth XXXXXXXXX 20XX, Accepted Xth XXXXXXXXX 20XX
DOI: 10.1039/b000000x

The diiron unit is commonly found as the active site in enzymes that catalyze important biological transformations. Two μ-(hydr)oxo-diiron(III) complexes with the ligands 2,2'-(2-methyl-2-(pyridine-2-yl)propane-1,3-diyl)bis(azanediyl)bis(methylene)diphenol (H_2L) and 2,2'-(2-methyl-2(pyridine-2-yl)propane-1,3diyl)bis(azanediyl) bis(methylene)bis(4-nitrophenol) (H_2L^{NO2}), namely $[(FeL)_2(\mu\text{-}O)]$ (**2**) and $[(FeL^{NO2})_2(\mu\text{-}OH)]ClO_4$ (**5**) were synthesized and characterized. In the solid state, both structures are asymmetric, with unsupported (hydr)oxo bridges. Intramolecular hydrogen bonding of the ligand NH groups to the phenolate O atoms hold the diiron cores in a bent configuration (Fe-O-Fe angle of 143.7° for **2** and 140.1° for **5**). A new phenolate bridged diferrous complex, $[(FeL)_2]$ (**4**), was synthesized and characterized. Upon exposure to air the diferrous **4** complex is oxidized to the diferric **2**. Cyclic voltammetry at different scan rates and chemical reduction of $[(FeL)_2(\mu\text{-}OH)]BPh_4$ (**1**) with cobaltocene revealed disproportionation followed by proton transfer, and a mixed-valence species could not be trapped. Subsequent exposure to molecular oxygen results in the formation of **2**. Electrochemical studies of **5** indicate easier reduction of the diiron(III/III) to the mixed-valence state than for **1**. The protonation of **2** by benzoic acid to form $[(FeL)_2(\mu\text{-}OH)]^+$ only changes the Fe-O-Fe angle by 5° (from 143.7° to 138.6°), and the pK_a of the hydroxo bridge is estimated to be about 20.4. We attribute this high pK_a partly to stabilization of the benzoate by hydrogen bonding to the ligand's amine proton. Magnetic susceptibility studies on solid samples of **1** and **2** yielded values of the antiferromagnetic exchange coupling constants, J, for these $S = 5/2$ dimers of -13.1 cm^{-1} and -87.5 cm^{-1}, respectively, typical of such unsupported hydroxo- and oxo-bridges.

Introduction

The (hydr)oxo-bridged diiron unit is commonly found in active sites of many proteins and has therefore attracted attention of bioinorganic chemists for the past couple of decades.[1-3] Besides the bridging O(H), these types of active sites have additional bridging ligands, such as aspartate or glutamate, plus other non-bridging ligands including histidine, glutamate, and/or aspartate. Proteins like soluble methane monooxygenase (sMMO),[4, 5] ribonucleotide reductase (RNR)[6] and hemerythrin (Hr)[7] have been thoroughly studied, and most of their structure-function relationships are understood.[8]

The transformation between the hydroxo- and oxo-bridged states of these active sites is of great importance.[9-12] In fact, several studies have suggested that proton transfer plays an important role in O–O bond cleavage in sMMO and RNR as part of the catalytic cycle.[13-15] The first known instance in which an oxo bridge in a diiron complex was protonated was shown in a model for Hr by Armstrong and Lippard.[16] However, very little has been reported about the actual pK_a's of bridging units in biological systems and model compounds.[17, 18]

While much emphasis has been placed on modeling the active sites of the aforementioned proteins,[1, 3, 6] enzymes containing asymmetric active sites, such as rubrerythrin and purple acid phosphatase, have received less attention, likely due to the fact that they are more difficult to model. A notable characteristic of these enzymes is that they go through a mixed-valence, Fe^{III}/Fe^{II}, intermediate in the course of their catalytic cycle.[19, 20] There are only a few examples of characterized μ-(hydr)oxo-diiron(III/II) model complexes, all having the same ligand, 1,4,7-trimethyl-triazacyclononane (Me_3TACN), but with various bridging ligands. Thus far, only one μ-OH mixed-valence complex has been reported by Wieghardt and coworkers, namely $[Fe^{III}Fe^{II}(Me_3TACN)_2(\mu\text{-}OH)(\mu\text{-}piv)_2](ClO_4)_2$ (piv = pivalate).[21] This complex has been both structurally and spectroscopically characterized, although it is very unstable. Two μ-O mixed-valence complexes have been reported.[22, 23] In 1987 Hartman and coworkers characterized a μ-O(μ-OAc)$_2$ mixed-valence species *in situ* by EPR and Mössbauer spectroscopy.[22] About ten years later, Hagen's research group structurally characterized a μ-O(μ-$O_2CCPh_3)_2$ mixed-valence complex, and provided extensive

spectroscopic evidence, including resonance Raman.[23, 24] Given the fact that there are only a few mixed-valence intermediates for μ-(hydr)oxo-diiron complexes, it is obvious that they are difficult to access and study, and the question arises, do proteins somehow allow for stabilization of these states?

The Houser laboratory previously reported the synthesis and coordination chemistry of the ligands shown in Scheme 1, specifically 2,2'-(2-methyl-2-(pyridine-2-yl)propane-1,3-diyl)bis(azanediyl)bis(methylene)diphenol (abbreviated H_2L)[25] and 2,2'-(2-methyl-2(pyridine-2-yl)propane-1,3diyl)bis(azanediyl) bis(methylene)bis(4-nitrophenol) (abbreviated H_2L^{NO2}).[26] These ligands share the same N_3O_2 donor set—one pyridyl N donor, two amine N donors, and two phenol O donors—and are dianionic upon deprotonation of the phenol OH groups. Also previously presented by our group was the synthesis and initial characterization of the asymmetric, unsupported hydroxo-bridged diiron(III) complex $[(FeL)_2(\mu\text{-}OH)]BPh_4$ (**1**) and the oxo-bridged $[(FeL^{tBu})_2(\mu\text{-}O)]$.[27] Here, we report our attempts to synthesize a mixed-valence complex by the reduction of **1**, the determination of the pK_a of the hydroxo bridge of **1**, two new diiron complexes with H_2L, and one new diiron complex with H_2L^{NO2}. Additionally, we present the magnetic properties of **1** and $[(FeL)_2(\mu\text{-}O)]$ (**2**).

Results and Discussion

Synthesis

Scheme 1 summarizes the syntheses and reaction pathways of **2**, $[FeL(CH_3OH)]$ (**3**), $[(FeL)_2]$ (**4**), $[(FeL^{NO2})_2(\mu\text{-}OH)]ClO_4$ (**5**), and their relationship to **1**. Two of our new complexes, **2** and **5**, are asymmetric, unsupported (hydr)oxo-bridged diiron(III) complexes like the previously synthesized **1**.[27] The asymmetry is caused by the unique hydrogen bonding within our ligand manifold, which helps to support the dimeric structure, yet also introduces angle strain into the Fe-O(H)-Fe bridge.

For this work, our preparation of **1** differed slightly from what was previously published.[27] Upon deprotonation of H_2L in CH_3OH, a solution of ferric perchlorate was added. After counterion metathesis with $NaBPh_4$, the complex precipitated out of solution. It was then dried, redissolved in dichloromethane, and recrystallized by vapor diffusion with pentane to obtain **1**·CH_2Cl_2, in contrast to the previous synthesis where it was crystallized from methanol and **1**·CH_3OH was isolated.[27] Conversion between **1** and **2** was achieved via (de)protonation, and **2** can also be obtained by reducing **1** with cobaltocene in dichloromethane solution, followed by decomposition according to Scheme 2 (*vide infra*). **5** was produced by treating H_2L^{NO2} with ferric perchlorate in the presence of Et_3N in methanol.

The ferrous complex **3** was synthesized by treatment of H_2L with NaH to deprotonate the phenol groups, followed by reaction with $FeCl_2$ or $Fe(OTf)_2$ in methanol. The formulation of this complex as **3** or $[\mathbf{3}]_2$ was verified by elemental analysis. However, when **3** was recrystallized from CH_3CN, the diferrous complex **4** was obtained. The crude powder from which **4** was crystallized is likely either a monomer with CH_3OH in the sixth coordination position or a dimer with two molecules of methanol hydrogen bonded to the complex. However, even after drying under high vacuum and heat the solvent molecule could not be removed, which favors the monomer formulation.

A solution of complex **3** in CH_2Cl_2 rapidly reacts with O_2 to give **2**. This reaction was monitored by UV-visible spectroscopy where a change in absorption from 471 nm to 420 nm with a strong increase in absorptivity occurs (see electronic supplementary information, Fig. S1). Similar reactions have been observed by others, and mechanistic pathways proposed.[3]

In a separate experiment, complex **3** was prepared in methanol and immediately exposed to air. Diethyl ether diffusion under atmospheric conditions gave crystals of $[(FeL)_2(\mu\text{-}OH)]OTf$. The formation of the hydroxo-bridged complex over the oxo-bridged is not surprising due to the high basicity of **2**. Electrospray mass spectra of solutions of **3** only show *m/z* = 879.2606, which corresponds to the protonated oxygenated product, $[(FeL)_2(\mu\text{-}OH)]^+$. The coordination of tetradentate salen ligands to the Fe^{II}-ion and the ability of the phenolate-O to act as a bridging unit has been studied recently and similar O_2 reactivity was shown.[28]

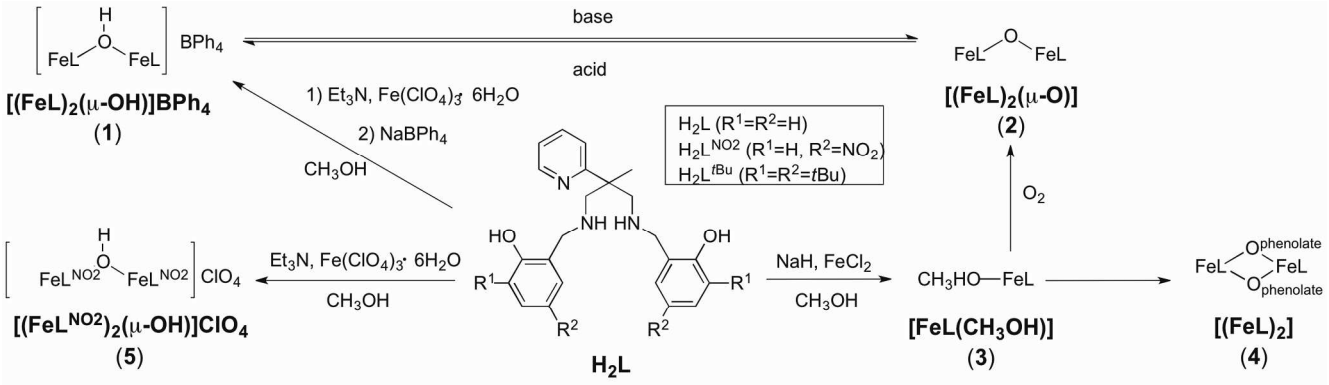

Scheme 1 Structures of ligands H_2L, H_2L^{NO2} and H_2L^{tBu} and the synthesis of iron complexes.

X-ray structures

Previously complex **1** was crystallized from methanol to yield **1**·CH_3OH.[27] In this work it was crystallized by diffusion of pentane into a dichloromethane solution of the complex, giving **1**·CH_2Cl_2, which has similar structural parameters (see Fig. S2 and Table 1). Like **1**·CH_3OH and **1**·CH_2Cl_2, the crystal structures of **2** and **5** show coordination to each ferric ion through all donor atoms of the pentadentate ligands $(L)^{2-}$ and $(L^{NO2})^{2-}$, respectively, and exhibit the same kind of intramolecular hydrogen bonding between the two subunits. A (hydr)oxo ligand acts as the sixth donor and bridges between the two ferric ions.

On the other hand, the diferrous complex **4** is doubly bridged

through one of the phenolate O-donors from each ligand, resulting in six-fold coordination of the metal center and the absence of any additional ligands. All of our μ-OH complexes are able to hydrogen bond to a solvent molecule via one of the amine N–H groups and the bridging OH ligand. In **1**, methanol is trapped, while in **5** water is present. Similarly, the N–H of **2** hydrogen bonds to acetone. This phenomenon is discussed in detail later.

[(FeL)$_2$(μ-O)] (**2**). The neutral complex **2** (Fig. 1) shows distorted octahedral coordination around the Fe^{III} centers, utilizing the N_3O_2 donors from $(L)^{2-}$ and the O from a bridging oxo ligand. Again, as in **1**,[27] the coordination environment around each iron site differs. While Fe1 has the oxo bridge O1 trans to the pyridine nitrogen N18A, Fe2 has the oxo bridge O1 *trans* to the amine nitrogen N20B. This results in slightly different Fe–donor bond lengths on the two different sites, as can be seen in Table 1. In order to distinguish the two iron sites, the terms Fe–O$^{trans\text{-py}}$ and Fe–O$^{cis\text{-py}}$ are used: Fe–O$^{trans\text{-py}}$ refers to the iron ion having the pyridine-N atom *trans* to the μ-O(H) and Fe–O$^{cis\text{-py}}$ refers to the iron ion having the pyridine-N atom *cis* to the μ-O(H).

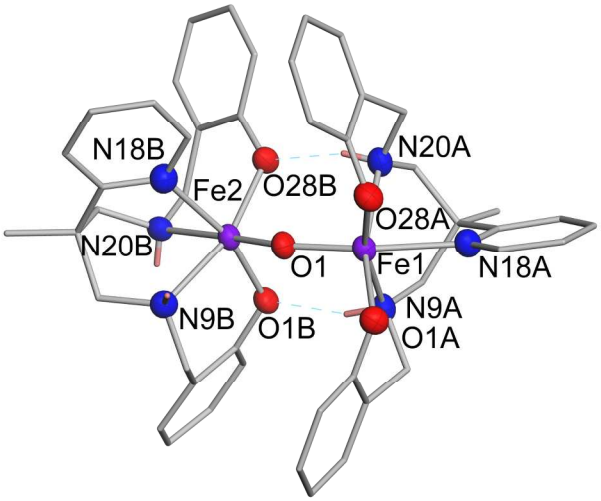

Fig. 1 Representation of the X-ray structure of **2** with all H atoms except the N9 and N20 amine H atoms removed for clarity. H-bonding interactions are represented by dashed lines. Selected bond lengths (Å): Fe1–O1A 1.9675(17), Fe1–O28A 2.0003(17), Fe1–N9A 2.227(2), Fe1–N20A 2.254(2), Fe1–N18A 2.273(2); Fe2–O28B 1.9785(18), Fe2–O1B 1.9967(17), Fe2–N9B 2.186(2), Fe2–N18B 2.231(2), Fe2–N20B 2.238(2).

In stark contrast to **1**, the Fe–O1 bond lengths in **2** for each subunit are very similar, with 1.8194(16) Å for Fe1–O1 and 1.8156(16) Å for Fe2–O1. ~~It is likely that the stronger antiferromagnetic coupling through an oxo vs. a hydroxo bridge compensates for the asymmetric charge distribution of the individual units.~~ Overall, the Fe–O1 bonds in **2** are shorter than in **1**, which can be explained by the greater electrostatic interaction between iron(III) and an oxo donor compared to iron(III) and hydroxo. The hydrogen bonding between the amine NH groups and phenolate O groups (N9A···O1B and N20A···O28B) most likely causes the bent structure in **2** with a Fe1–O1–Fe2 bond angle of 143.71(10)°. Due to this unique intramolecular hydrogen bonding, the bridging angle in **2** is only 5° more obtuse than in our OH-bridged complex **1**.[27] Most unsupported oxo-bridged diferric complexes have Fe-O-Fe angles of 160° to 180°,[1] with a few exceptions having Fe-O-Fe angles of 139° – 145°.[29-32] Our previously synthesized O-bridged complex with the same ligand backbone (but *t*Bu-substituted) does not show intramolecular hydrogen bonding between the two subunits, and the bridging angle is nearly linear with a Fe-O-Fe bond angle of 169.4(6)°.[27] The only other example where the bridging angle does not change significantly compared to its hydroxo-bridged analogue was reported for the heme-like unsupported structure (μ-oxo)bis(tetraphenylporphyrinato)iron(III), which is sterically hindered.[33] While unsupported oxo-bridged diferric complexes are usually rather linear, it is common for complexes with additional carboxylato bridges to range in Fe–O–Fe angles from 118-138°, depending on the kind and number of bridging ligands.[1]

[(FeL^{NO2})$_2$(μ-OH)]ClO$_4$ (**5**). The X-ray structure of **5** (Fig. 2) also reveals a dimeric structure with two distinct coordination environments around each iron center, which is caused by the same difference in orientation of the ligands due to hydrogen bonding interactions between the two subunits that was mentioned earlier. The structure of **5** is very similar to **1** but the counter ion in **5** is perchlorate. As in **1**,[27] the bond lengths of the hydroxo O-atom to Fe^{III} are different for each site with Fe1–O1 being 1.9688(16) Å and Fe2–O1 being 2.0029(16) Å. Both bonds are significantly shorter than in **1** (see Table 1). This is probably due to the electron withdrawing properties of the nitro-substituted ligand, which cause a slightly higher positive charge on the iron(III) ion and therefore stronger interactions with the bridging hydroxo ligand. Similar to **1**, the different coordination environment around each iron center in **5** produces different bond lengths for the Fe–donor bonds as can be seen in Fig. 2. **5** has a Fe–O–Fe bond angle of 140.06(9)° which is similar to the Fe-O-Fe angle of 138.64(9)° found in **1**.

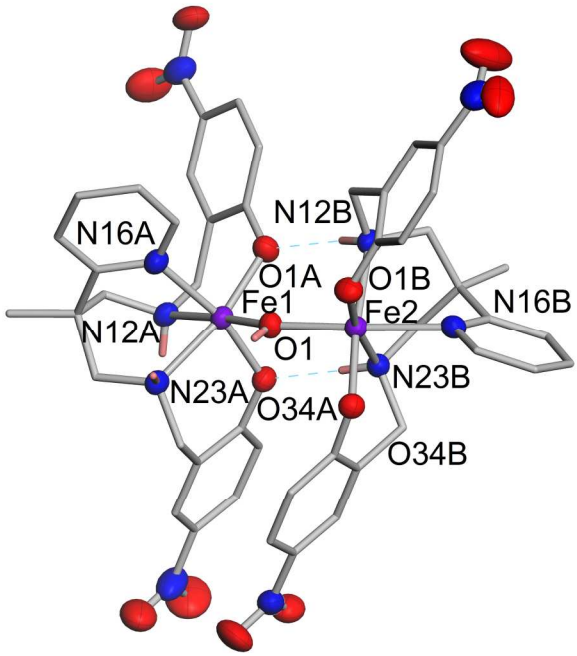

Fig. 2 Representation of the X-ray structure of the cationic portion of **5** with all H atoms except the N12B and N23B amine and μ-hydroxo H atoms removed for clarity. H-bonding interactions are represented by

dashed lines. Selected bond lengths (Å): Fe1–O1A 1.9318(16), Fe1–O34A 1.9554(16), Fe1–N16A 2.1716(19), Fe1–N23A 2.1720(19), Fe1–N12A 2.1721(18); Fe2–O1B 1.9131(15), Fe2–O34B 1.9311(15), Fe2–N12B 2.1687(19), Fe2–N23B 2.1760(18), Fe2–N16B 2.1988(19).

Table 1 Comparison of Fe–O–Fe core unit parameters.

Complex	Fe–O–Fe (deg)	Fe–O$^{trans\text{-}py}$ (Å)	Fe–O$^{cis\text{-}py}$ (Å)	Fe···Fe (Å)	reference
$[(FeL)_2(\mu\text{-}OH)]BPh_4\cdot CH_3OH$	138.64(9)	2.0174(16)	2.0033(17)	3.7616(7)	[27]
$[(FeL)_2(\mu\text{-}OH)]BPh_4\cdot CH_2Cl_2$	138.96(6)	2.0292(11)	1.9901(11)	3.7643(4)	this work
$[(FeL^{NO2})_2(\mu\text{-}OH)]ClO_4$	140.06(9)	2.0029(16)	1.9688(16)	3.7329(4)	this work
$[(FeL)_2(\mu\text{-}O)]$	143.71(10)	1.8194(16)	1.8156(16)	3.4542(7)	this work
$[(FeL^{tBu})_2(\mu\text{-}O)]$	169.4(6)	1.844(10)[a]	1.793(10)[a]	3.621(4)	[27]
$[(FeL)_2]$	N/A	N/A	N/A	3.3545(9)	this work

[a]In complex $[(FeL^{tBu})_2(\mu\text{-}O)]$ both pyridine ligands are trans to the oxo bridge.

$[(FeL)_2]$ (4). The ligand $(L)^{2-}$ is the only donor in the structure of **4** (see Fig. 3), thus resulting in distorted octahedral coordination via the bridging abilities of the ligand. The N_3O_2 donor set accounts for pentadentate coordination, and one phenolate O-atom of each ligand bridges to the adjacent iron ion resulting in overall six-coordinate high-spin iron(II) centers. This kind of metal bridging ability of the phenolate ligand is very common.[25, 34-37] **4** is a neutral complex and contains an inversion center which allows transformation of equivalent atoms via –x+1, –y+1, –z+1. Although it is common for phenolate to act as a bridging moiety between two metal centers, to the best of our knowledge, diferrous bis(μ-phenoxy) complexes with an additional N3 donor around each iron center have not been reported thus far. Yet, N_2O_2 reduced Schiff base iron(II) complexes have been synthesized where two phenolate anions act as bridges between the two irons, resulting in overall pentadentate coordination around the metal center.[28]

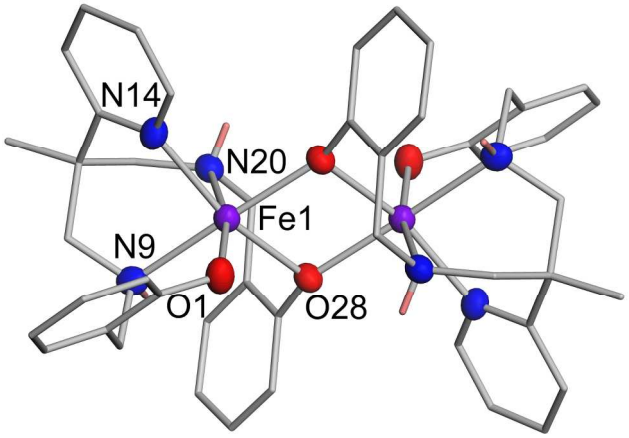

Fig. 3 Representation of the X-ray structure of **4** with all H atoms except the N9A and N20A amine H atoms removed for clarity. Selected bond lengths (Å) and angles (deg): Fe1–O1 2.0159(17), Fe1–O28 2.1307(17), Fe1–O28#1 2.1328(17), Fe1–N14 2.194(2), Fe1–N9 2.248(2), Fe1–N20 2.288(2); Fe1–O28–Fe1#1 103.77(7).

Hydrogen bonding pocket. Complexes **1**, **2**, and **5** have the capacity to form H-bonds acceptor (Lewis base) molecules. **1** was previously synthesized from methanol and shows hydrogen bonding to methanol via the ligand N–H and the bridging O–H hydrogen bond donors. The H-acceptor atom from the solvent molecule forms a six-membered ring with the complex unit (Fig. 4). However, when **1** is recrystallized from CH_2Cl_2/pentane, the pocket is open and no guest molecule is observed in the solid state. Instead, CH_2Cl_2 occupies other lattice space within the crystal. Similar to **1**, **5** also has a solvent molecule trapped in the pocket, but in this case it is water instead of methanol.

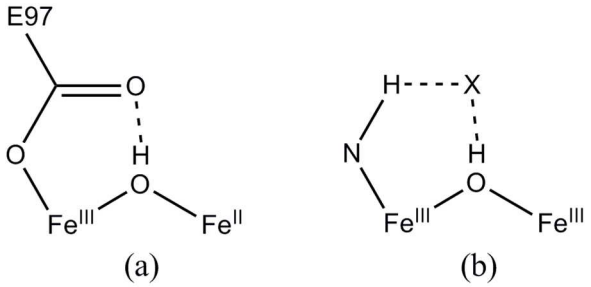

Fig. 4 Schematic depiction of H-bonding within the hydroxo-bridged diiron unit; (a) Mixed-valence intermediate in rubrerythrin.[38] (b) diiron(III) center in **1** and **5** (X = H-bond acceptor).

In contrast to **1** and **5**, **2** only exhibits one H-bond donor, which is the ligand N–H, and when **2** is recrystallized from wet acetone/pentane, one molecule of acetone accepts the hydrogen bond, and a molecule of water and a second acetone are present elsewhere in the crystal lattice. If one considers the space-filling model (Fig. S3), clearly the O-bridge seems sterically inaccessible and probably this is the reason why the highly basic O-bridge does not get protonated by the water present in solution. On the other hand, when crystals are crushed up and dried under high vacuum, elemental analysis matches best with a formula of **2**·H_2O.

Our H-bonding pocket, when occupied by an H-bond acceptor, X, can be compared to the H-bonding configuration in the mixed-valence state of the active site of rubrerythrin (Rbr).[19, 38] It seems likely that H-bonding with glutamate (E97) stabilizes the mixed-valence state in the enzyme by preventing proton transfer. Studies of Rbr mutants revealed that E97, which seems to be unique to this enzyme, is essential for the formation of a mixed-valence intermediate.[39] Model studies conducted by Wieghardt and colleagues show that proton transfer from the bridging (hydr)oxo ligand is a key step in disproportionation.[21] This suggests that an appropriate H-bond acceptor, X, might be able to trap the bridging proton in our complexes, thereby preventing proton exchange and ultimately stabilizing a mixed-valence state.

Spectroscopic and physical properties

UV-visible spectroscopy. The UV-visible spectrum of **1** exhibits three distinct bands in the range of 200 to 1000 nm (Fig. S4). The near-UV features are assigned as π–π^* transitions of the

phenolate groups.[40] The high energy transition (shoulder ~320 nm) is assigned to the CT from the out of plane $p\pi$ orbital (HOMO) of the phenolate oxygen to the d-orbital of the iron center. The low energy band (475-550 nm) arises from the in-plane $p\pi$ orbital (POMO) of the phenolate to the d π^* orbital of the iron(III) ion.[41] The position and intensity of the LMCT band is sensitive to the coordination environment of the iron center.[42] In **1**, the purple color, and therefore the band at around 500 nm, brings to mind the CT band of purple acid phosphatase's active site which is located at 510-560 nm.[42] This is not surprising due to similarities in ligands that cause the CT band (phenolate here vs. tyrosinate in PAP).

In **2** the two high energy bands are similar to **1**. The iron ion in **2** is a weaker Lewis acid than in **1** because of the stronger electron donation from the oxo ligand vs. the hydroxo ligand. Thus the *d* orbitals in **2** are higher in energy and create a greater energy gap for the LMCT (phenolate to iron) resulting in a blue shift (from 496 nm to 412 nm).[43] There is only a slight increase in absorption for **2** compared to **1**, which is reasonable considering that the overall coordination is similar. The decrease of the Fe–O bond length in **2** compared to **1** most likely causes the higher probability for the LMCT due to greater overlap of the orbitals. The significant difference in the absorption maximum of the POMO band in **1** compared to **2** makes it convenient to monitor the interconversion of the two complexes by UV-visible spectroscopy.

The absorption spectrum of **5** is dominated by a broad band at 380 nm with significantly higher molar absorptivity than seen in **1**. This band is mainly assigned to π–π^* transition within the nitrophenolate unit.[44] Most likely this band covers the higher energy LMCT. The lower energy LMCT is shifted to higher energy and also falls into the broad high absorbing feature.[45] The fact that the band at 380 nm masks the absorption features, which reflect the nature of the coordination environment around the metal center, does not allow for pK_a determination via UV-visible titrations (*vide infra*).

Magnetic properties. The molar susceptibility vs. temperature plot for **1** (Fig. 5) shows a gradual increase in χ_M with deceasing temperature, leading to a broad maximum between 100 and 40 K, that is typical of weakly antiferromagnetically coupled S = 5/2 Fe^{III} centers. The χ_M values below the maximum are heading towards zero, as expected for an S = 0 coupled ground state[46] but increase rapidly below ~3 K because of traces of monomeric S = 5/2 'impurities'. The corresponding $\chi_M T$ vs. T values (Fig. 6) show a steady and rapid decrease from 5.8 $cm^3\ mol^{-1}$ K at 300 K (μ_{eff} = 6.81 μ_B per Fe_2; 4.82 μ_B per Fe) towards 0 $cm^3\ mol^{-1}$ K at 0 K except for the leveling off below 3 K due to monomer impurity.

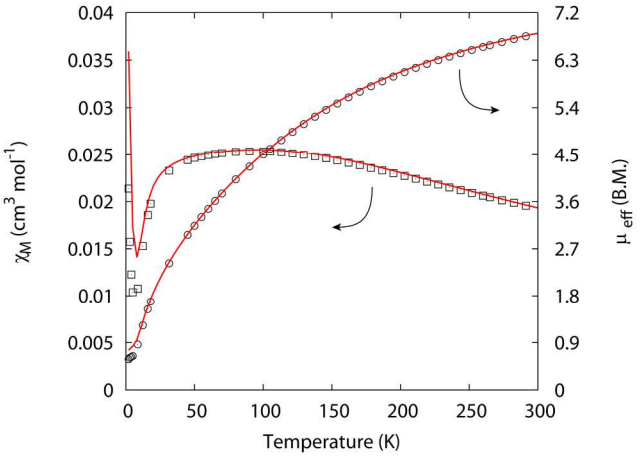

Fig. 5 Squares: plot of χ_M (per Fe_2) vs. temperature (K) for the powdered sample of **1**·2H_2O in applied field of 0.5 T; the red line is the best-fit as described in the script. Circles: plot of μ_{eff} vs. temperature (K) with the red line using the same best-fit parameters as in the χ_M plot.

The data were fitted extremely well to a Heisenberg spin Hamiltonian $-2J\mathbf{S_1}.\mathbf{S_2}$[46] using program PHI.[47] The best-fit parameter set is g = 2.00, J = –13.1 cm^{-1}, and monomer impurity = 2%. The next highest spin state above the ground S = 0 ground state is S = 1 at 26.2 cm^{-1}. The analogous crystalline sample **1**·CH_2Cl_2 shows essentially the same magnetic behaviour as the powder sample (Fig. S4) with best-fit parameters g = 1.99, J = –12.9 cm^{-1}, and monomer impurity = 3%.

Comparison of these J values to those reported for other Fe^{III}-OH-Fe^{III} complexes reveals that, up until ~1990, dibridged $Fe(OH)_2Fe$ complexes[1] were reported to have J values of –7 to –12 cm^{-1} while tri-bridged $Fe(OH)(RCO_2)_2Fe$ species[1] have J values of –17 cm^{-1}. A recent $Fe(OH)_2Fe$ example [(Hbpbp)Fe(μ-$OH)_2$]$(ClO_4)_4$·2C_3H_6O, where Hbpbp = 2,6-bis((*N*,*N*-bis-(2-picolyl)amino)methyl)-4-*tert*-butylphenol showed J = –8 cm^{-1}.[48]

Some singly OH-bridged complexes have been reported recently with, for example, bis-porphyrin complexes having Fe-O-Fe bridge angles of ~142° (c/f/ 139° here) and J reported to be between –4 to –42 cm^{-1}, this remarkable range being ascribed to the counteranions (I_3^-, BF_4^-, ClO_4^-) playing a key, size related, role.[49] Earlier, the octaethylporphyrin complex ([Fe(OEP)]$_2$(μ-OH)(ClO_4) was crystallized but J could not be obtained because of impurities.[50] The porphyrin complexes[49] showed hydrogen bonded interactions to the OH hydrogen, as also occurs in the case of **1** crystallized from methanol, but, while they can play a part, it seems unlikely these intermolecular interactions could yield such large differences in J values. The co-ligands, namely porphyrins and L, can influence J values, although the core bridging moiety, such as in the μ-oxo FeOFe families[1, 46] usually dominates with porphyrin co-ligands giving larger negative values than other chelators, the majority of which give similar J's. A singly OH-bridged Schiff base complex [{(saltenFe)$_2$(μ-OH)}(BPh_4).$(MeCN)_x$.$(H_2O)_y$, where salten^{2-} = 4-azaheptane-1,7,-bis(salicylaldiminate), yielded a J of –21 cm^{-1} (159° bridging angle) the size of which could be reproduced well by DFT calculations.[51] This result is broadly in agreement with the present [(FeL)$_2$(μ-OH)]BPh_4 complex, the slightly stronger coupling in the Schiff base complex suggesting that the Fe-O(H)-Fe bridge angle plays a part in the net J value.

The plot of χ_M vs. T for the complex **2** is typical of those for oxo-bridged $Fe^{III}OFe^{III}$ complexes[1,3,45] and is shown in Fig. 6. The $\chi_M T$ value at 300 K of 0.48 cm^3mol^{-1} K, per Fe, (μ_{eff} = 1.96 μ_B) decreases ~linearly towards zero (as does the susceptibility), because of population of the S = 0 coupled ground state. Below ~50 K there is a Curie-like S = 5/2 magnetic impurity of 0.2%, a quite common feature in such dinuclear compounds. Fitting of the data for **2** using the 5/2:5/2 model[1,45] yielded J = –87.5 cm^{-1} and g = 1.99 (Fig. 6). Oxo-bridged complexes are known to show –J values between 80-120 cm^{-1} and porphyrine-ligated species have slightly higher values (120-140 cm^{-1}).[1, 52] Typically, for unsupported (μ-oxo)diiron(III) compounds J lies in the range of –80 to –105 cm^{-1} and (μ-oxo)bis(μ-carboxylato)diiron(III) compounds have values of about –120 cm^{-1}.[22, 53] It is common that upon deprotonation of the hydroxo bridge the strength of antiferromagnetic exchange increases by an order of magnitude due largely to the shorter Fe-O bond length in FeOFe species, combined with changes in Fe..Fe separation and Fe-O-Fe angle.[54] From a chemical perspective, μ-OH bridges yield poorer superexchange pathways than do μ-O bridges.

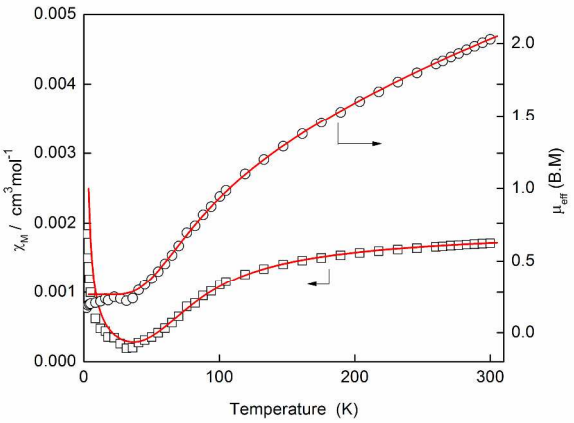

Fig. 6. Squares: plot of χ_M (per Fe) vs. temperature (K) for the powdered sample of **2** in applied field of 0.5 T; the solid line is the best-fit as described in the script. Circles: plot of μ_{eff} vs. temperature (K) with the solid line using the same best-fit parameters as in the χ_M plot.

In order to authenticate the species present in solution, the magnetic moment data for **1** and **2** were determined using the Evans method.[55, 56] The magnetic moment, μ_{eff}, for **1** at 294 K was measured in $CDCl_3$, and was determined to be 5.82 μ_B per Fe_2 or 4.12 μ_B per Fe. These values are reasonably close to the measurement in the solid state, which when corrected for temperature are 6.74 μ_B per Fe_2 or 4.77 μ_B per Fe. The magnetic moment for **2** was similarly measured in $CDCl_3$ using the Evans method at 294 K. The solution μ_{eff} for **2** was determined to be 3.09 μ_B per Fe_2 or 2.19 μ_B per Fe, which compares to the values of 2.74 μ_B per Fe_2 or 1.94 μ_B per Fe at the same temperature in the solid state. Both of these solution magnetic measurements support the notion that the dimeric forms of **1** and **2** are the primary species in solution.

Overall, the magnetic behavior of **1** and **2** is similar to that observed previously for unsupported (hydr)oxo-bridged diferric complexes. A recent theoretical study on oxo-carboxylato bridged species reveals that superexchange pathways mostly mediate through the oxo-bridge, whereas only one out of six exchange pathways arises from bridging acetate groups.[54]

Acid–base properties. Preliminary exploration of the acidity of **1**[27] suggested that it has a very high pK_a because it did not appear to be completely deprotonated by either triethylamine or proton sponge (pK_a values in CH_3CN = 18.82 and 18.62, respectively).[57] Our investigations corroborated those initial results. Under atmospheric conditions, addition of approximately 2700 equivalents of Et_3N to **1** shifted the peak maximum from 496 nm to 480 nm. An additional 2700 equivalents caused a further shift to 435 nm, but still not all the way to 412 nm (λ_{max} observed for **2** in CH_3CN). Titrations with proton sponge yielded similar results, so we concluded that the pK_a of the hydroxo bridge must be significantly higher than 18.

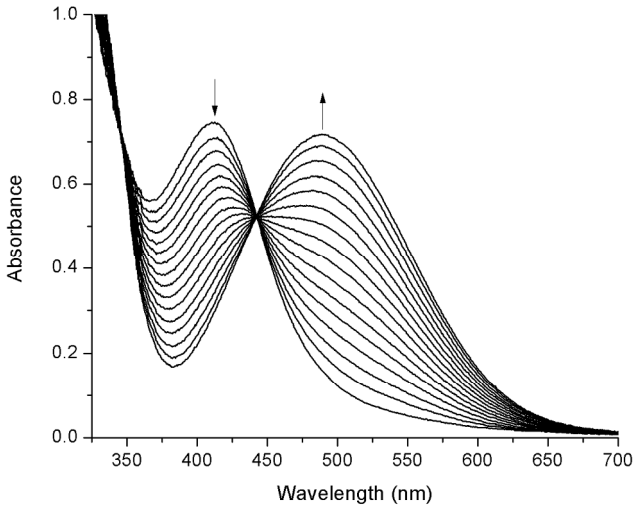

Fig. 7 Titration of **2** (9.1 x 10^{-5} M) with up to 2.5 equivalents of benzoic acid in CH_3CN to generate $[(FeL)_2(\mu\text{-}OH)]^+$ monitored by UV-visible spectroscopy.

Better results were achieved using 1.1-1.2 equivalents of 1,8-diazabicyclo[5.4.0]undec-7-ene (DBU; pK_a in CH_3CN = 24.34)[57] or 1,1,3,3-tetramethylguanidine (TMG; pK_a in CH_3CN = 23.3).[58] These experiments were, however, also performed under atmospheric conditions, and after the initial deprotonation with addition of the base, we observed that the peak began to shift back toward its original position, suggesting that the complex was becoming protonated again. This made it impractical to obtain accurate calculations from these data, but by performing the titrations piecemeal rather than continuously to compensate for the peak shift, we were able to estimate the pK_a to be in the range of 22-23. The presence of water would still make this result artificially high, an idea supported by subsequent experiments.

In order to avoid further complications, solid benzoic acid, which is easier to dry, was selected and solutions were prepared in a glove box under nitrogen. Air-free titrations of **2** with benzoic acid (HOBz) were monitored by UV-visible spectroscopy (Fig. 7). An air-free titration of **2** with benzoic acid shifted the peak from 412 nm to 489 nm, with an isosbestic point at 442 nm. Though 489 nm is slightly different than 496 nm, as is usually observed for **1** in acetonitrile, in this case the counter ion is benzoate rather than tetraphenylborate, which would accept a hydrogen bond from the bridging O–H, thus slightly weakening

its bond strength and thereby slightly changing the coordination environment of the iron ions. The precise isosbestic point at 442 nm is evidence that no other side reactions were occurring, such as the coordination of benzoic acid to the iron centers.

The equilibrium constant, K_{eq}, was calculated at several points throughout the titration, based on the change in absorbance at 505 nm, because that region of the spectrum showed the greatest change. K_{eq} is defined as:

$$K_{eq} = \frac{[[(FeL)_2(\mu\text{-}OH)]^+][OBz^-]}{[[(FeL)_2(\mu\text{-}O)]][HOBz]} \quad (1)$$

The change in absorbance makes it possible to determine the fraction of the complex that still exists as **2** and how much has been converted to $[(FeL)_2(\mu\text{-OH})]^+$ at any given point in the titration, because the complex is assumed to exist entirely as **2** at the beginning of the titration and $[(FeL)_2(\mu\text{-OH})]^+$ at the end. $[OBz^-]$ is then assumed to be equal to $[[(FeL)_2(\mu\text{-OH})]^+]$, and [HOBz] is assumed to be equal to the amount of benzoic acid added at that point, minus $[OBz^-]$.Then, the K_a of the complex was calculated from Eq. 2:[59, 60]

$$K_a(\text{complex}) = K_a(\text{acid})/K_{eq} \quad (2)$$

where K_a (acid) = 3.09 x 10^{-22} (pK_a = 21.51) in acetonitrile.[61] The titration was performed in triplicate (Fig. S5), and K_a(complex) was calculated at several different points between the start and endpoint of each titration, and the average value for each titration was determined. The average of those values is 5.3 ± 1 x 10^{-22} (pK_a = 21.3 ±0.1).

However, the values calculated from different points within the same titration, rather than showing random variability due to error, showed a trend. The value calculated for the pK_a increased as the titration progressed. This makes sense, because as more benzoic acid is added, more benzoate is available to hydrogen bond to the bridging hydroxo proton and to the amine proton, as illustrated in Figure 4. This has the effect of making the protonated form even more stable, and thus raising the apparent pK_a. The actual pK_a can be estimated by plotting the observed pK_a vs. the quantity of benzoic acid added to the system (Fig. S6). The y-intercept represents the theoretical pK_a if no benzoic acid had been added; in this case, 20.4. A similar analysis of the other two titrations gave values of 20.3 and 20.6, respectively. Even though these estimates are lower than the values calculated by averaging all of the various determinations of K_a(complex), they are still unusually high values, even for a diiron complex. The closest values we have observed in the literature were published by Zheng, *et al*., for their series of complexes with (μ-oxo)(μ-hydroxo)diiron(III) cores, having pK_a values ranging from 15.9 to 17.6.[60] It has been observed that phenolates are more strongly electron donating than pyridine and other N-donor ligands, which would result in more electron density on the iron centers.[62] This may be an important factor contributing to the high pK_a that we observe.

Chemical reduction of 1. From the previously published cyclic voltammogram (CV) of **1**[27] (see Fig. 9), we estimated the stability of a potential mixed-valence complex (Fe^{II}/Fe^{III}) using Eq. 3:

$$K_c = 10^{\Delta E/59mV} = \left[M^{(n-1)}\right]^2 \div \left[M\right]\left[M^{(n-2)}\right] \quad (3)$$

where K_c is the comproportionation constant (higher values indicate a more stable mixed-valence complex) and ΔE represents the difference between two redox couples (here diferric/mixed-valence and mixed-valence/diferrous).[63, 64]

Using a ΔE value for **1** of 670 mV, K_c was estimated to be 10^{11} for the mixed-valence $[(FeL)_2(\mu\text{-OH})]$. This should be a reasonably stable mixed-valence complex, and the crystal structure of **1** suggests that a localized mixed-valence complex might form upon reduction due to the different coordination environments around each iron center. Cobaltocene ($CoCp_2$) is an appropriate reductant according to its high reduction potential of –1.33 V vs. Fc (in CH_2Cl_2),[65] and the fact that its potential lies in between the two metal-centered redox couples at –1.04 V and –1.72 V. The reaction of the purple complex **1** with $CoCp_2$ in CH_2Cl_2 resulted in a color change to yellow-orange and the formation of a yellow precipitate which was filtered off and identified as $[CoCp_2]BPh_4$ by ^{1}H NMR and X-ray diffraction. After removal of the solvent, a crude orange precipitate was isolated and, unexpectedly, diferric **2** was obtained after recrystallization in the presence of air.

To further investigate the formation of **2** upon reduction of **1**, a titration study was conducted in CH_3CN. After addition of $CoCp_2$ solution to **1**, the band at 496 nm in the UV-visible spectrum disappears while a new band grows in at 412 nm. Three isosbestic points can be observed. The absorption at 412 nm has about half of the intensity as the band at 496 nm after the addition of one equivalent of reductant (Fig. 8). The side product $[CoCp_2]BPh_4$ only adds slightly to the band at 412 nm (see Fig. S7, absorption spectrum of $[CoCp_2]BPh_4$). After exposure to O_2, the new band at 412 nm increases in intensity by about twofold without a significant shift in λ_{max}. Based on these observations, it appears that half an equivalent of **2** is formed after reduction of one equivalent of **1**, and then subsequent exposure to O_2 leads to all material being converted to **2**.

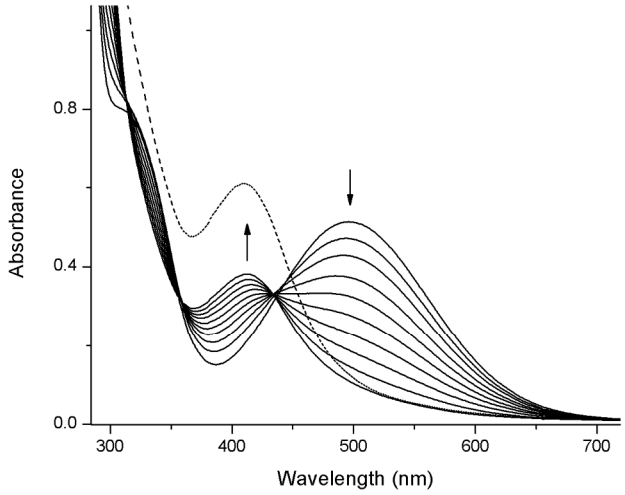

Fig. 8 Titration of **1** (7.3 x 10^{-5} M) with up to one equivalent of $CoCp_2$ in CH_3CN monitored by UV-visible spectroscopy (solid lines) and subsequent addition of O_2 (dashed line).

Cite this: DOI: 10.1039/c0xx00000x

www.rsc.org/xxxxxx

ARTICLE TYPE

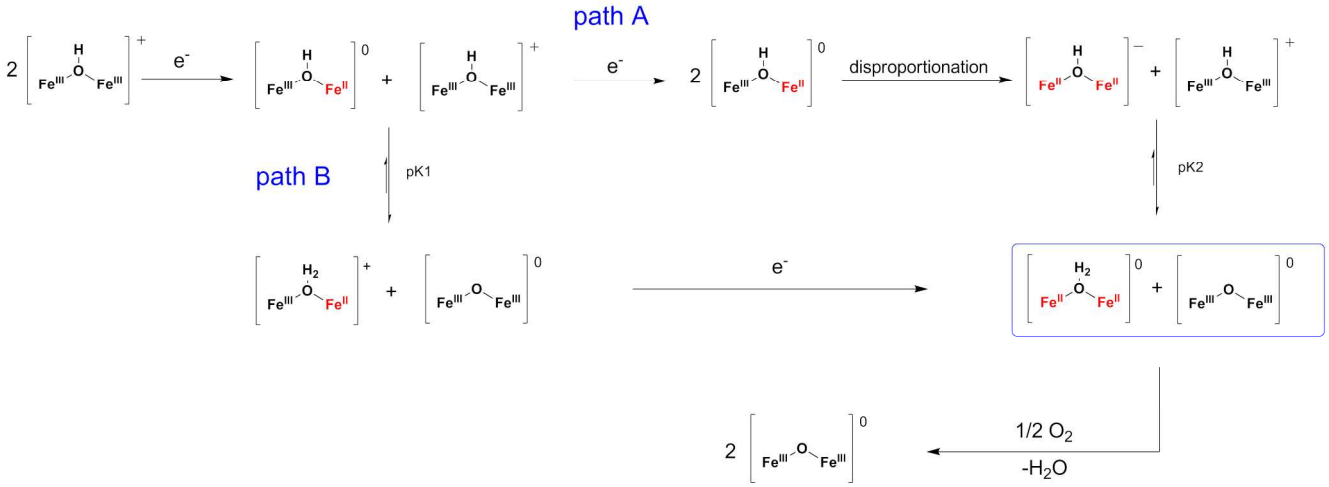

Scheme 2 Proposed mechanism for the disproportionation of **1** upon reduction.

Inspired by the mechanistic characterization by Wieghardt and coworkers,[21] the mechanism depicted in Scheme 2 is proposed whereby **1** is reduced to form diferric **2** and diferrous $[(FeL)_2(\mu\text{-}OH_2)]$ (see blue box in Scheme 2). The typically pale diferrous species barely contributes to the UV-visible absorption.[21] Two paths, A and B, are outlined in the scheme. In path A, two equivalents of $[(FeL)_2(\mu\text{-}OH)]^+$ are reduced, which results in the formation of two equivalents of mixed-valence $[(FeL)_2(\mu\text{-}OH)]$. Disproportionation may then occur, yielding diferric $[(FeL)_2(\mu\text{-}OH)]^+$ and diferrous $[(FeL)_2(\mu\text{-}OH)]^-$. The p$K_a$ of the differic complex should be lower (its bridging-oxygen atom is less basic because more electron density is shared with the iron(III) centers) than that of the diferrous complex, which causes formation of **2** and $[(FeL)_2(\mu\text{-}OH_2)]$ (see blue box). The alternate path for decomposition is shown in path B. It is possible that upon addition of substoichiometric amounts of reductant, some of the mixed-valence complex $[(FeL)_2(\mu\text{-}OH)]$ is formed. When mixed-valence $[(FeL)_2(\mu\text{-}OH)]$ and unreacted $[(FeL)_2(\mu\text{-}OH)]^+$ are in close proximity, proton transfer may occur from the ferric to the mixed-valence complex due to a difference in pK_a, resulting in products $[(FeL)_2(\mu\text{-}OH_2)]^+$ and **2**. With the addition of another electron, it is probably more likely to reduce the cationic species. This results, again, in formation of the same products shown in the blue box in Scheme 2.

The difference between the two paths is that path A follows a disproportionation reaction, while in path B, two separate reductions occur. Both paths may yield in the same products. Moreover it could be that both paths occur simultaneously and even more equilibria between different species are transpiring. If path B is very fast, and path A may be thermodynamically not as favorable, it could be possible to trap the mixed-valence complex by fixation of the bridging hydroxo proton. The proper hydrogen bonded host molecule, X, may hold the proton in position. This could allow for isolation and characterization of the mixed-valence complex.

When O_2 is added after formation of **2** and ($[(FeL)_2(\mu\text{-}OH_2)]$ (see blue box in Scheme 2), more **2** is formed from the reaction of the diferrous complex with dioxygen. The oxo-bridged dimer has an about 1.2-fold higher absorption than the hydroxo-bridged complex; this explains the difference in intensities in the final spectrum. Even under argon at –78°C, no other intermediates were observed when **1** was treated with cobaltocene.

The reaction pathway upon reduction of **1** is in good agreement with the work done by Wieghardt and coworkers, who trapped an OH-bridged mixed-valence species and followed its decomposition to the oxo-bridged complex.[21] Yet, it is surprising that the mixed-valence product from the reduction of **1** is so unstable compared to Wieghardt's complex, which is stable for about half an hour at room temperature.

Electrochemistry. The redox behavior of **1** in methylene chloride was previously described.[27] In this work, all complexes are explored through cyclic voltammetry in acetonitrile solutions and the CV of **1** was repeated in acetonitrile in order to allow for reasonable comparison. Similar to what was seen in methylene chloride, complex **1** exhibits two quasi-reversible metal-centered reductions at $E_{½}$ = –1052 (ΔE = 131 mV) and $E_{½}$ = –1724 (ΔE = 192 mV) vs. ferrocene. These redox couples were initially assigned to the $Fe^{III}Fe^{III}/Fe^{II}Fe^{III}$ and $Fe^{II}Fe^{III}/Fe^{II}Fe^{II}$ couples, respectively. At positive potentials an irreversible ligand-centered oxidation is found at +356 mV (Fig. 9).

In contrast, **2** shows only one quasi-reversible reduction feature at $E_{½}$ = –1824 (ΔE = 246 mV) assigned to the $Fe^{III}Fe^{III}/Fe^{II}Fe^{III}$ redox couple. The second reduction feature is not accessible due to the limitations of the solvent window. There

is also one irreversible feature at +145 mV that corresponds to ligand oxidation (see Fig. 9). The shift in potential of the differic to ferrous/ferric couple for **2**, compared to that of **1**, seems reasonable because the oxo ligand in **2** causes higher electron density at the metal centers and therefore a more negative reduction potential.

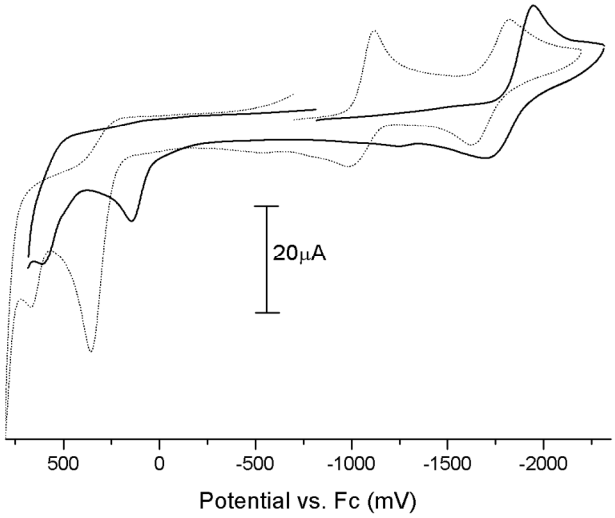

Fig. 9 Cyclic voltammograms (scan rate = 100 mV s^{-1}; 0.1 M $TBAPF_6$ supporting electrolyte) of 1.0 mM solutions of **1** (dotted line) and **2** (solid line) in CH_3CN.

The electrochemical behavior of **2** upon treatment with acid was investigated in order to validate the benzoic acid titrations that were tracked by UV/visible spectroscopy (see previous section). An acetonitrile solution of **2** generated in situ by exposure of **4** to oxygen was scanned from +1.0 V to –2.0 V vs. ferrocene. The initial CV displays the same quasi-reversible redox couple centered at –1824 mV. Upon addition of aliquots of trifluoroacetic acid, two new redox features appear at around –1100 mV and –1700 mV. As more acid is added to the solution, the intensity of these features increase, and the intensity of the redox couple at around –1800 mV decreases. The two new features correspond closely to the redox couples measured for hydroxo-bridged **1**. These results reinforce the evidence from UV/visible spectroscopic titrations of **2** with benzoic acid that oxo-bridged **2** can be protonated in solution to generate hydroxo-bridged **1**.

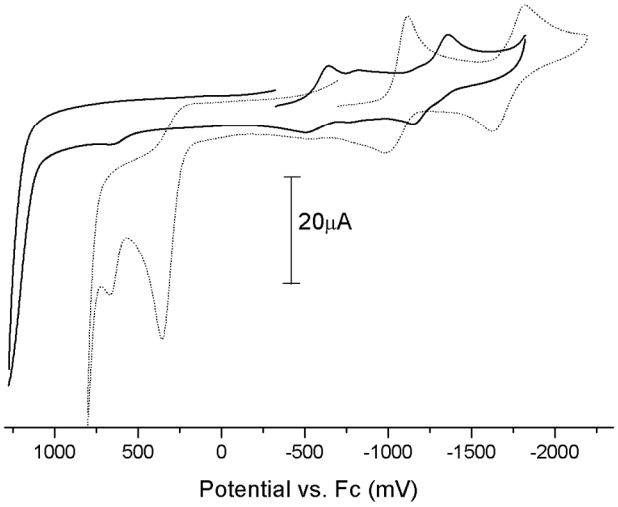

Fig. 10 Cyclic voltammograms (scan rate = 100 mV s^{-1}; 0.1 M $TBAPF_6$ supporting electrolyte) of 1.0 mM solutions of **1** (dotted line) and **5** (solid line) in CH_3CN.

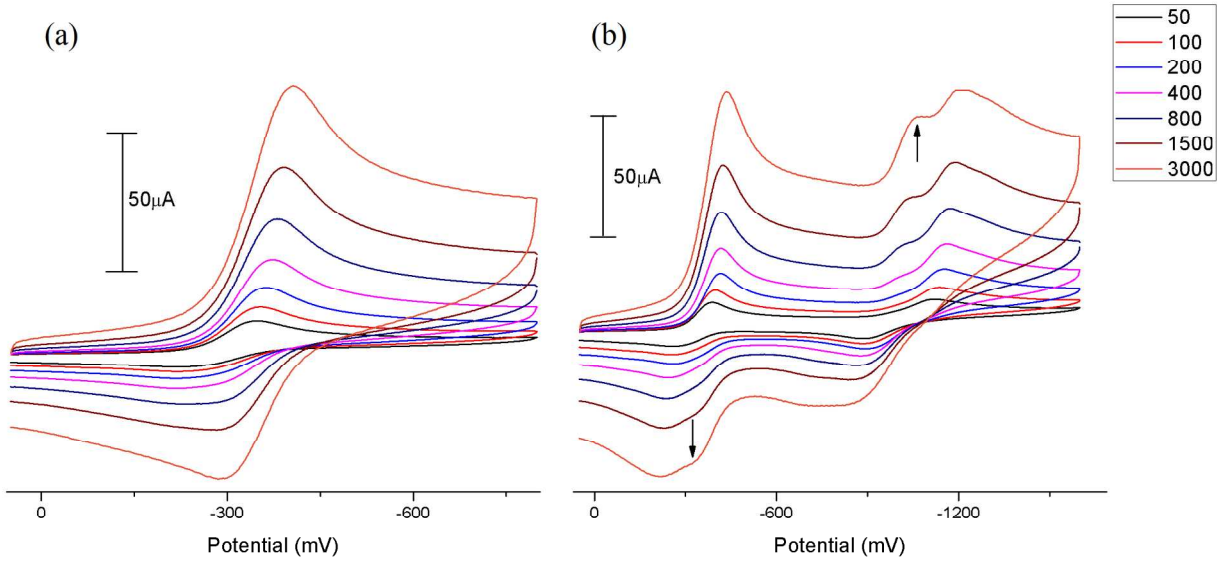

Fig. 11 Cyclic voltammograms of the metal-centered features of **1** at different scan rates in CH_3CN (0.1 M $TBAPF_6$ supporting electrolyte, 1.0 mM solutions of **1**). (a) Scan window from +50 to –800 mV and (b) from +50 to –1600 mV.

Initial CV studies on powdered **5** having sufficient purity (according to elemental analysis) show similar redox features to $[(FeL)_2(\mu\text{-}OH)]BPh_4$. The metal-based redox couples are shifted 475 mV more positive (see Fig. 10). This shift is reasonable due to the electron-withdrawing nature of the nitro-substituted ligand, resulting in more positive iron centers and thus more favorable

reduction. No oxidative processes were observed within the solvent window of CH_3CN.

Further studies on the electrochemistry of **1** using different scan rates revealed more complex behavior. The first redox couple, assigned to Fe^{II}/Fe^{III}, is chemically irreversible because $I_{pa}/I_{pc} \sim 0.5$. At faster scan rates the back oxidation seems more reversible (see Fig. 11), suggesting a secondary reaction upon reduction of $[(FeL)_2(\mu\text{-OH})]^+$. Scanning to more negative potentials reveals the second redox feature, which upon further analysis at varying scan rates appears to be more complex than we initially thought. When the scan rate is increased additional peaks appear in the CV (see Fig. 11). We believe that the new reduction peak at –1100 mV is actually related to the Fe^{III}/Fe^{II} to Fe^{II}/Fe^{II} couple. At low scan rates this peak is not observed because of the quick disproportionation of the mixed-valence complex. The peak centered at –1200 mV is more likely to be the Fe^{III}/Fe^{III} to Fe^{III}/Fe^{II} couple of $[(FeL)_2(\mu\text{-O})]$, which is one of the direct products of disproportionation described here. The new oxidative peak at –400 mV could be assigned to an oxidation of the diferrous complex. We cannot calculate a new comproportionation constant, K_c, without knowing which peaks exactly correspond to the Fe^{III}/Fe^{II} to Fe^{II}/Fe^{II} couple. However, since the new peaks at faster scan rates lie at more positive potential, one can say that the separation of the two metal centered redox couples is smaller than estimated before and hence K_c will be smaller. This would be in agreement with the high instability of the purported mixed-valence species.

Finally, the electrochemical properties of **4** were probed by cyclic voltammetry. In contrast to **1**, **2** and **5**, which all contain an oxo- or hydroxo bridge, **4** was expected to exhibit different electrochemical properties due to its ligand-based phenolato bridging oxygens. The CV for **4** (Fig. S9) shows two redox couples, the first at –410 mV and the second at –978 mV (both vs. ferrocene), that are shifted to more positive potentials relative to **1**, **2** and **5**. The couples at –410 mV and –978 mV are likely associated with the Fe^{III}/Fe^{III} to Fe^{III}/Fe^{II} couple and the Fe^{III}/Fe^{II} to Fe^{II}/Fe^{II} reductions, respectively. The appearance of small features around –630 mV and –1460 mV upon exposure to air indicates that **4** rapidly reacts with oxygen, corroborating the known extreme air sensitivity of **4**. Allowing the solution of **4** to stir under air eventually leads to the CV of **2**, confirming that the oxo-bridged **2** can be generated from **4** (see Scheme 1).

Conclusions

In summary, we report the synthesis and characterization of new complexes, which model aspects of the active sites of asymmetric (hydr)oxo-bridged diiron containing enzymes. Our complexes show unique intramolecular hydrogen bonding which supports the bridging (hydr)oxo group and holds the iron units together in a bent configuration. De/protonation does not affect the bridging angle significantly. We discovered an H-bonding pocket at the differic center that mimics the configuration in the mixed-valence state of rubrerythrin's active site. Acid–base UV-visible titrations result in an estimate for the pK_a of the hydroxo bridge that is very high (~20.4), which may be caused in part by the H-bonding behavior. Furthermore, on the basis of cobaltocene titrations, we suggest that **1** disproportionates upon one electron reduction and, following proton exchange, produces **2**. This behavior is consistent in both chemical and electrochemical reduction experiments. A reasonable mechanism for the decomposition is presented in Scheme 2. Electrochemical studies of **5** suggest that it is easier to reduce, and ongoing experiments will explore its potential to form a mixed-valence complex. Additionally, different H-bond acceptors, X, will be investigated, and their ability to stabilize a mixed-valence state evaluated. These studies will help to reveal the role H-bonding between Glu97 and the diiron core in rubrerythrin. Magnetochemical studies on the μ-OH and μ-O crystalline complexes give values of the exchange coupling constant, J, that are typical of these bridging moieties in dinuclear iron(III) compounds.

Experimental

General

Unless otherwise stated, all reagents were used as received from commercial sources. 2-methyl-2-(pyridine-2-yl)propane-1,3-diamine (ppda) was synthesized according to the published procedure.[66] H_2L and H_2L^{NO2} were synthesized according to the published procedures.[25, 26] Solvents used were doubly purified using alumina columns in an MBraun solvent purification system (MB-SPS). Infrared spectra were measured from 4000 to 400 cm^{-1} as KBr pellets, suspensions in Nujol, or solutions on a Bio-Rad FTS155 FTIR spectrometer. ^1H NMR spectra were measured using a Varian 300 MHz instrument using solvent as an internal standard. Mass spectra were measured on a Q-TOF quadrupole time-of-flight mass spectrometer (Micromass, Manchester, U.K.) equipped with a Z-spray electrospray ionization (ESI) source. Elemental analyses were performed by Atlantic Microlab, Norcross, GA. UV-visible pK_a-titrations were performed using a Shimadzu UV2401PC spectrophotometer and for all other spectral data collection a Hewlett Packard 8453 spectrophotometer was used in the range 200 to 1000 nm on solutions ranging in concentration from 1.0×10^{-3} M to 1.0×10^{-5} M. Cyclic voltammetry experiments were performed using a BAS 50W potentiometer and a standard three-electrode cell with a glassy-carbon working electrode, a Pt-wire auxiliary electrode, and an Ag pseudo reference electrode under an inert atmosphere at room temperature. Magnetic susceptibility data on ~25 mg polycrystalline samples were obtained using a Quantum Design MPMS5 Squid magnetometer with the accurately weighed sample contained in a gel capsule that was held in a soda straw that was fixed to the end of the sample rod. The applied dc field was 0.5 T. The instrument was calibrated using a pellet of Pd of accurately known magnetisation, supplied by Quantum Design, and checked against chemical calibrants such as $CuSO_4 \cdot 5H_2O$ and $Hg[Co(NCS)_4]$.

Syntheses

Caution! *Perchlorate salts of metal complexes with organic ligands are potentially explosive. Although no difficulty was encountered during the syntheses described herein, complexes should be prepared in small amounts and handled with caution.*

$[(FeL)_2(\mu\text{-OH})]BPh_4$ (1) *via* alternate route. The synthesis of **1** was varied slightly to the previously published.[27] $Fe(ClO_4)_3 \cdot 6H_2O$ (0.143 g, 0.310 mmol) in methanol (1 mL) was added to a methanolic solution (10 mL) of ligand (0.117 g, 0.310 mmol) and NEt_3 (0.075 g, 0.691 mmol) and the solution

subsequently turned dark wine-red. After stirring for one hour at room temperature, solid $NaBPh_4$ (0.160 g, 0.468 mmol) was added and a purple precipitate formed immediately. The slurry was refluxed overnight and the purple precipitate collected by filtration. The crude powder of **1** was obtained (180 mg, 94%) after washing with methanol and diethyl ether and drying. **1**·$2H_2O$: $C_{70}H_{75}BFe_2N_6O_7$ (1234.88): calcd. C 68.08, H 6.12, N 6.81; found C 68.17, H 5.91, N 6.47.

The crude powder was dissolved in CH_2Cl_2 and a small amount of insoluble residue removed by filtration through celite. After pentane diffusion into the dichloromethane filtrate, a microcrystalline dark purple solid, **1**·CH_2Cl_2**,** was obtained which was collected and dried. This material was suitable for X-ray diffraction study. Crystalline **1**·CH_2Cl_2: $C_{71}H_{73}BCl_2Fe_2N_6O_5$ (1283.78): calcd. C, 66.43; H, 5.73; N, 6.55; found C, 66.81; H, 5.74; N, 6.54. UV-visible (CH_3CN): λ_{max} (ε, $M^{-1}cm^{-1}$) = 496 (7,000) nm.

[(FeL)$_2$(μ-OH)]OTf. In yet another route to $[(FeL)_2(\mu\text{-OH})]^+$, **3** was generated *in situ* upon addition of $Fe(OTf)_2$ to a methanol solution of deprotonated ligand (as described in the synthesis of **4**) and immediately exposed to air. When trying to crystallize the reaction product through diethyl ether diffusion, the solution was kept under atmospheric conditions and crystals of $[(FeL)_2(\mu\text{-OH})]OTf$ were obtained.

[(FeL)$_2$(μ-O)] (**2**). **1**·$2H_2O$ (149.5 mg, 0.121 mmol) was dissolved in CH_2Cl_2 (14 mL), and to this stirring solution $CoCp_2$ (23.6 mg, 0.125 mmol) in CH_2Cl_2 (1 mL) was added. The color changed immediately from dark purple to orange with formation of some yellow precipitate. The solution was stirred for 15 more minutes and diethyl ether (30 mL) was added to complete the precipitation. The reaction was worked up under air. The yellow precipitate (58 mg, 0.114 mmol, 94%) was isolated after filtration and identified by NMR spectroscopy as well as X-ray diffraction as $CoCp_2BPh_4$. ^1H NMR (300 MHz, d–acetone, 293K) δ 5.88 (s, 10H, Cp^-), 6.78 (t, 4H, *p*-BPh_4), 6.93 (t, 8H, BPh_4), 7.34 (m, 8H, BPh_4). In a different experiment single crystals of $CoCp_2BPh_4$ were obtained from a dilute reaction solution.

The filtrate was then concentrated in high vacuum and a crude powder of **2** was obtained (110 mg, 0.120 mmol, 99%). **2**·$2H_2O$: $C_{46}H_{54}Fe_2N_6O_7$ (914.65): calcd. C 60.40, H 5.95, N 9.19; found: C 60.50, H 6.22, N 8.74. Single crystals (41%) suitable for X-ray diffraction were obtained after vapor diffusion of pentane into acetone solution of crude **2**. **2**·H_2O: $C_{46}H_{52}Fe_2N_6O_6$ (896.63): calcd. C 61.62, H 5.85, N 9.37; found: C 61.63, H 6.08, N 9.20. UV-visible (CH_2Cl_2): λ_{max} (ε, $M^{-1}cm^{-1}$) = 235 (35,100), 270 (28,000), 420 (7,900) nm; (CH_3CN) = 412 (8,400) nm. FTIR (CH_2Cl_2): $\tilde{\nu}$ = 3686, 3605, 3277, 3048, 2913, 2860, 1714, 1593, 1566, 1481, 1454, 1359, 1292, 874, 596 cm^{-1}; (Nujol): 3250, 3111, 3057, 2958, 2922, 2851, 1714, 1638, 1593, 1566, 1481, 1454, 1359, 1287, 1225, 1072, 1013, 879, 757 cm^{-1}. ESI-MS (CH_2Cl_2): m/z = 431.1301 $[FeL]^+$, 879.2593 $[(FeL)_2(\mu\text{-OH})]^+$.

[(FeL)$_2$] (**4**). NaH (18 mg, 0.750 mmol) in methanol (0.5 mL) was added dropwise to a solution of H_2L (140 mg, 0.371 mmol) in methanol (4 mL), and stirred for a few minutes. $FeCl_2$ (47 mg, 0.371 mmol) in CH_3OH (0.5 mL) was added dropwise to the ligand solution and the color of the solution turned orange-red with some precipitate. The solution was immediately filtered through glass wool followed by continued stirring of the filtrate. Formation of more precipitate started after 30 min., but the solution was allowed to stir overnight to complete precipitation. The precipitate was collected through filtration, washed with methanol and diethyl ether and dried. A pink powder was obtained (110 mg, 0.237 mmol) in 64 % yield. Elemental analysis suggests that the crude material is LFe with CH_3OH as a coordinating solvent (methanol did not leave after drying under high vacuum). $C_{24}H_{29}FeN_3O_3$ (463.35): calcd. C 62.21, H 6.31, N 9.07; found: C 62.65, H 6.32, N 9.18. UV-visible (CH_2Cl_2): λ_{max} (ε, $M^{-1}cm^{-1}$) = 471 (1,000) nm. FTIR (KBr): $\tilde{\nu}$ = 3278, 3253, 2857, 1593, 1476, 1450, 1279, 1108, 1032, 872, 755 cm^{-1}. ESI-MS (CH_2Cl_2): m/z = 431.1291 $[FeL]^+$, 879.2496 $[(FeL)_2(\mu\text{-OH})]^+$. Recrystallization of the crude powder was obtained through slow evaporation of a CH_3CN solution to yield **4**. A solution of **4** in dichloromethane, when exposed to air shifts in absorption from λ_{max} = 471 nm to 420 nm , which corresponds to **2**.

[(FeL^{NO2})$_2$(μ-OH)]ClO$_4$ (**5**). H_2L^{NO2} (0.060 g, 0.128 mmol) was dissolved in a mixture of methanol and dichloromethane (3:1 mL) and deprotonated with NEt_3 (0.030 g, 0.295 mmol). $Fe(ClO_4)_3$·$6H_2O$ (0.060 g, 0.130 mmol) in methanol (1 mL) was added to the ligand solution and the solution subsequently turned orange with immediate formation of dark brown-orange precipitate. After stirring over night at room temperature the solid was collected by filtration and washed with methanol and diethyl ether. Crude powder of **5** was obtained (27 mg, 36% yield). **5**·$2H_2O$: $C_{46}H_{51}ClFe_2N_{10}O_{19}$ (1195.10): calcd. C 46.23, H, 4.30, N 11.72; found C 46.53, H 4.09, N 11.67. UV-visible (CH_3CN): λ_{max} (ε, $M^{-1}cm^{-1}$) = 380 (54,860) nm. FTIR (KBr): $\tilde{\nu}$ = 2371, 2345, 1599, 1479, 1436, 1333, 1290, 1119, 1093, 926, 836, 784, 759, 669 cm^{-1}. ESI-MS (CH_3CN): m/z = 521.0993 $[FeL^{NO2}]^+$, 1059.2016 $[(FeL^{NO2})_2(\mu\text{-OH})]^+$. Crystalline material of **5** was obtained upon diffusion of CH_2Cl_2 into a solution of crude material in CH_3CN.

Titrations

Titration of 1 with base. Et_3N was added in 100 μL aliquots (2700 equivalents each) to an acetonitrile solution of **1** (7.5×10^{-5} M). Solution of proton sponge in acetonitrile (3.3×10^{-2} M) was added in increments of 500 equivalents to an acetonitrile solution of **1** (8.6×10^{-5} M). Acetonitrile solutions of DBU or TMG (8.6×10^{-3} M) were added to an acetonitrile solution of **1** (8.6×10^{-5} M) in increments of 0.1 equivalent of base up to 1.2 equivalents, then in increments of 1 equivalent up to 4 equivalents. In all cases, a UV-visible spectrum was recorded after each addition of base to the sample.

Titration of 2 with benzoic acid. Acetonitrile solutions of **2** (9.1×10^{-5} M) and of benzoic acid (9.1×10^{-4} M) were prepared under nitrogen atmosphere. The solution of **2** was placed in a cuvette fitted with a septum, and the benzoic acid solution was introduced in increments of 0.08 equivalents of benzoic acid to **2** using an airtight syringe. The temperature was held constant at 25° C.

Titration of 1 with cobaltocene. Air-free titrations of **1** with $CoCp_2$ were monitored by UV-visible spectroscopy in CH_3CN. Solutions of **1** (7.3×10^{-5} M, 3.25 mL) in a gas tight cuvette capped with a septum and $CoCp_2$ (2.5×10^{-3} M, 100 µL) in an airtight gas syringe were prepared in a dry box under nitrogen. The $CoCp_2$ solution was added in aliquots of 11 μL to the solution of **1** and a UV-visible spectrum was collected after each

addition. A total of one equivalent reducing agent was added to the diiron solution. Subsequently 0.5 mL of oxygen was added to the reacted solution and a final spectrum collected (see Fig. 8).

X-ray crystal structure determination

X-ray quality crystals of **1**·CH_2Cl_2 were obtained by diffusion of pentane into a methylene chloride solution of **1**. Single crystals of **2** were obtained by slow evaporation of pentane into an acetone solution of **2**. Single crystals of **4** were obtained by slow evaporation of an acetonitrile solution of **4**. Single crystals of **5** were obtained by slow evaporation of methylene chloride into a solution of **5** in acetonitrile. Intensity data for all the compounds were collected using a diffractometer with a Bruker APEX ccd area detector[67, 68] and graphite-monochromated Mo-*K*α radiation (λ = 0.71073 Å). The samples were cooled to 100(2) K. Cell parameters were determined from a non-linear least-squares fit of the data. The data were corrected for absorption by the semi-empirical method.[69]

Table 2 Crystallographic data for **2**, **4**, and **5**.

	2·2C_3H_6O·H_2O	**4**·2CH_3OH	**5**·H_2O·C_2H_3N·CH_2Cl_2
formula	$C_{52}H_{64}Fe_2N_6O_8$	$C_{48}H_{58}Fe_2N_6O_6$	$C_{49}H_{54}Cl_3Fe_2N_{11}O_{18}$
fw	1012.79	926.70	1303.08
Crystal system	triclinic	monoclinic	monoclinic
Space group	$P\bar{1}$	$P2_1/n$	$P2_1/n$
a (Å)	11.074(2)	12.8640(18)	11.9637(6)
b (Å)	12.872(2)	13.4112(19)	20.2286(11)
c (Å)	17.425(3)	13.0923(19)	22.2512(12)
α (deg)	84.588(4)	90	90
β (deg)	86.831(4)	103.606(3)	95.204(2)
γ (deg)	83.527(5)	90	90
V (Å^3)	2454.5(7)	2195.3(5)	5362.8(5)
Z	2	2	4
ρ_{calcd} (mg/m^3)	1.370	1.402	1.614
μ (mm^{-1})	0.652	0.718	0.777
θ (deg)	1.160 to 28.318	1.997 to 28.406	1.838 to 28.338
$R1$,[a] $wR2$[b] [$I>2\sigma(I)$]	0.0503, 0.1204	0.0504, 0.1103	0.0484, 0.1184
GOF on F^2	1.013	1.006	1.004

The structures were solved by direct methods and refined by full-matrix least-squares methods on F^2.[70, 71] Hydrogen atom positions of hydrogen atoms bonded to carbon atoms were initially determined by geometry and were refined by a riding model. Hydrogen atoms bonded to nitrogen or oxygen atoms were located on a difference map, and their positions were refined independently. Non-hydrogen atoms were refined with anisotropic displacement parameters. Hydrogen atom displacement parameters were set to 1.2 (1.5 for methyl) times the displacement parameters of the bonded atoms. Crystal data for **2**·2C_3H_6O·H_2O, **4**·2CH_4O and **5**·H_2O·C_2H_3N·CH_2Cl_2 are summarized in Table 2. Selected bond lengths and angles for **2**, **4** and **5** are summarized in Table 1 and the figure captions for Figs. 1–3.

CCDC reference numbers 956271 (**1**), 956273 (**2**), 956272 (**4**), and 956270 (**5**). These data can be obtained free of charge from The Cambridge Crystallographic Data Centre via www.ccdc.cam.ac.uk/data_request/cif.

Acknowledgements

This work was supported by the National Science Foundation (NSF CHE-0616941, R.P.H.) and the Australian Research Council (K.S.M.). Additionally, we thank the NSF for the purchase of a CCD-equipped X-ray diffractometer at OU (CHE-0130835). We are grateful to Prof. George Richter-Addo for allowing access to instrumentation, Prof. Mike Shaw for fruitful discussions about the electrochemistry, and Prof. Richard Taylor for helpful consultation regarding the acid-base titrations.

Notes and References

[a] *Department of Chemistry & Biochemistry, University of Oklahoma, Norman, OK 73019, USA.*
[b] *Chemistry Department, Monash University, Clayton, Victoria 3168 Australia.*
[c] *Department of Chemistry & Biochemistry, University of Northern Colorado, Greeley, CO 80639, USA. Fax: +1 970 351 2176; Tel: +1 970 351 2877; E-mail: robert.houser@unco.edu*

† Electronic Supplementary Information (ESI) available: Crystallographic data in CIF format (www.ccdc.cam.ac.uk/data_request/cif), UV-visible spectra of **4** before and after exposure to O_2 (Fig. S1), representation of the X-ray structure of **1**·CH_2Cl_2 (Fig. S2), space-filling representation of **2** (Fig. S3), UV/visible spectrum of **1** in CH_3CN (Fig. S4), plot of molar susceptibility vs. temperature for cystalline **1**·CH_2Cl_2 (Fig. S5), change in absorbance of **2** with addition of benzoic acid (Fig. S6), plot of observed pK_a vs. the quantity of benzoic acid added to **2** (Fig. S7), UV-visible spectrum of $CoCp_2BPh_4$ (Fig. S8), and cyclic voltammogram of **4** (Fig. S9). See DOI: 10.1039/b000000x/

1. D. M. Kurtz, *Chem. Rev.*, 1990, **90**, 585-606.
2. L. Que and A. E. True, in *Prog. Inorg. Chem.*, John Wiley & Sons, Inc., 2007, pp. 97-200.
3. E. Y. Tshuva and S. J. Lippard, *Chem. Rev.*, 2004, **104**, 987-1012.
4. R. L. Lieberman and A. C. Rosenzweig, *Nature*, 2005, **434**, 177-182.
5. M. Merkx, D. A. Kopp, M. H. Sazinsky, J. L. Blazyk, J. Müller and S. J. Lippard, *Angew. Chem., Int. Ed.*, 2001, **40**, 2782-2807.
6. J. Du Bois, T. J. Mizoguchi and S. J. Lippard, *Coord. Chem. Rev.*, 2000, **200**, 443-485.
7. D. M. Kurtz Jr, in *Comprehensive Coordination Chemistry II*, eds. J. A. McCleverty and T. J. Meyer, Pergamon, Oxford, 2003, pp. 229-260.
8. E. I. Solomon, T. C. Brunold, M. I. Davis, J. N. Kemsley, S.-K. Lee, N. Lehnert, F. Neese, A. J. Skulan, Y.-S. Yang and J. Zhou, *Chem. Rev.*, 1999, **100**, 235-350.
9. M. J. Scott, H. H. Zhang, S. C. Lee, B. Hedman, K. O. Hodgson and R. H. Holm, *J. Am. Chem. Soc.*, 1995, **117**, 568-569.

10. R. E. Stenkamp, L. C. Sieker, L. H. Jensen, J. D. McCallum and J. Sanders-Loehr, *Proc. Natl. Acad. Sci. U. S. A.*, 1985, **82**, 713-716.
11. M. A. Holmes, I. Le Trong, S. Turley, L. C. Sieker and R. E. Stenkamp, *J. Mol. Biol.*, 1991, **218**, 583-593.
12. S. K. Ghosh and S. P. Rath, *J. Am. Chem. Soc.*, 2010, **132**, 17983-17985.
13. M. A. Cranswick, K. K. Meier, X. Shan, A. Stubna, J. Kaizer, M. P. Mehn, E. Münck and L. Que, *Inorg. Chem.*, 2012, **51**, 10417-10426.
14. S.-K. Lee and J. D. Lipscomb, *Biochemistry*, 1999, **38**, 4423-4432.
15. C. E. Tinberg and S. J. Lippard, *Biochemistry*, 2009, **48**, 12145-12158.
16. W. H. Armstrong and S. J. Lippard, *J. Am. Chem. Soc.*, 1984, **106**, 4632-4633.
17. W.-G. Han and L. Noodleman, *Dalton Trans.*, 2009, 6045-6057.
18. T. Lovell, J. Li and L. Noodleman, *Inorg. Chem.*, 2001, **40**, 5267-5278.
19. R. Iyer, R. Silaghi-Dumitrescu, D. Kurtz, Jr. and W. Lanzilotta, *J. Biol. Inorg. Chem.*, 2005, **10**, 407-416.
20. A. Vogel, F. Spener and B. Krebs, in *Encyclopedia of Inorganic and Bioinorganic Chemistry*, John Wiley & Sons, Ltd, 2011.
21. U. Bossek, H. Hummel, T. Weyhermüller, E. Bili and K. Wieghardt, *Angew. Chem., Int. Ed.*, 1995, **34**, 2642-2645.
22. J. A. R. Hartman, R. L. Rardin, P. Chaudhuri, K. Pohl, K. Wieghardt, B. Nuber, J. Weiss, G. C. Papaefthymiou, R. B. Frankel and S. J. Lippard, *J. Am. Chem. Soc.*, 1987, **109**, 7387-7396.
23. J. D. Cohen, S. Payne, K. S. Hagen and J. Sanders-Loehr, *J. Am. Chem. Soc.*, 1997, **119**, 2960-2961.
24. S. C. Payne and K. S. Hagen, *J. Am. Chem. Soc.*, 2000, **122**, 6399-6410.
25. R. Shakya, A. Jozwiuk, D. R. Powell and R. P. Houser, *Inorg. Chem.*, 2009, **48**, 4083-4088.
26. R. Shakya, Z. Wang, D. R. Powell and R. P. Houser, *Inorg. Chem.*, 2011, **50**, 11581-11591.
27. R. Shakya, D. R. Powell and R. P. Houser, *Eur. J. Inorg. Chem.*, 2009, 5319-5327.
28. C. J. Whiteoak, R. Torres Martin de Rosales, A. J. P. White and G. J. P. Britovsek, *Inorg. Chem.*, 2010, **49**, 11106-11117.
29. J. E. Davies and B. M. Gatehouse, *Acta Crystallogr. B*, 1973, **29**, 1934-1942.
30. M. C. Weiss and V. L. Goedken, *Inorg. Chem.*, 1979, **18**, 819-826.
31. M. Gerloch, E. D. McKenzie and A. D. C. Towl, *J. Chem. Soc. (A)*, 1969, 2850-2858.
32. R. Biswas, M. G. B. Drew, C. Estarellas, A. Frontera and A. Ghosh, *Eur. J. Inorg. Chem.*, 2011, 2558-2566.
33. D. R. Evans, R. S. Mathur, K. Heerwegh, C. A. Reed and Z. Xie, *Angew. Chem.*, 1997, **109**, 1394-1396.
34. K. R. Grünwald, M. Volpe and N. C. Mösch-Zanetti, *J. Coord. Chem.*, 2012, **65**, 2008-2020.
35. Y. Yahsi and H. Kara, *Inorg. Chim. Acta*, 2013, **397**, 110-116.
36. L. K. Das, A. Biswas, A. Frontera and A. Ghosh, *Polyhedron*, 2013, **52**, 1416-1424.
37. M. Novotný, Z. Padělková, J. Holeček and A. Růžička, *J. Organomet. Chem.*, 2013, **733**, 71-78.
38. D. M. Kurtz Jr, *J. Inorg. Biochem.*, 2006, **100**, 679-693.
39. E. D. Coulter, N. V. Shenvi, Z. M. Beharry, J. J. Smith, B. C. Prickril and D. M. Kurtz Jr, *Inorg. Chim. Acta*, 2000, **297**, 231-241.
40. K. Hasan, C. Fowler, P. Kwong, A. K. Crane, J. L. Collins and C. M. Kozak, *Dalton Trans.*, 2008, 2991-2998.
41. M. Palaniandavar, M. Velusamy and R. Mayilmurugan, *J. Chem. Sci.*, 2006, **118**, 601-610.
42. M. I. Davis, A. M. Orville, F. Neese, J. M. Zaleski, J. D. Lipscomb and E. I. Solomon, *J. Am. Chem. Soc.*, 2002, **124**, 602-614.
43. K. Ramesh and R. Mukherjee, *J. Chem. Soc., Dalton Trans.*, 1992, 83-89.
44. M. Merkel, F. K. Müller and B. Krebs, *Inorg. Chim. Acta*, 2002, **337**, 308-316.
45. R. Mayilmurugan, M. Sankaralingam, E. Suresh and M. Palaniandavar, *Dalton Trans.*, 2010, **39**, 9611-9625.
46. K. S. Murray, *Coord. Chem. Rev.*, 1974, **12**, 1-35.
47. N. F. Chilton, R. P. Anderson, L. D. Turner, A. Soncini and K. S. Murray, *J. Comput. Chem.*, 2013, **34**, 1164-1175.
48. M. Ghiladi, F. B. Larsen, C. J. McKenzie, I. Sotofte and J.-P. Tuchagues, *Dalton Trans.*, 2005, 1687-1692.
49. S. Bhowmik, S. K. Ghosh, S. Layek, H. C. Verma and S. P. Rath, *Chem. Eur. J.*, 2012, **18**, 13025-13037.
50. W. R. Scheidt, B. Cheng, M. K. Safo, F. Cukiernik, J. C. Marchon and P. G. Debrunner, *J. Am. Chem. Soc.*, 1992, **114**, 4420-4421.
51. J. Jullien, G. Juhász, P. Mialane, E. Dumas, C. R. Mayer, J. Marrot, E. Rivière, E. L. Bominaar, E. Münck and F. Sécheresse, *Inorg. Chem.*, 2006, **45**, 6922-6927.
52. I. M. Wasser, C. F. Martens, C. N. Verani, E. Rentschler, H.-w. Huang, P. Moënne-Loccoz, L. N. Zakharov, A. L. Rheingold and K. D. Karlin, *Inorg. Chem.*, 2003, **43**, 651-662.
53. F. J. Wu, D. M. Kurtz, K. S. Hagen, P. D. Nyman, P. G. Debrunner and V. A. Vankai, *Inorg. Chem.*, 1990, **29**, 5174-5183.
54. J. H. Rodriguez and J. K. McCusker, *J. Chem. Phys.*, 2002, **116**, 6253-6270.
55. D. F. Evans, *J. Chem. Soc.*, 1959, 2003-2005.
56. G. A. Bain and J. F. Berry, *J. Chem. Educ.*, 2008, **85**, 532.
57. I. Kaljurand, A. Kütt, L. Sooväli, T. Rodima, V. Mäemets, I. Leito and I. A. Koppel, *J. Org. Chem.*, 2005, **70**, 1019-1028.
58. I. M. Kolthoff, M. K. Chantooni and S. Bhowmik, *J. Am. Chem. Soc.*, 1968, **90**, 23-28.
59. M. Baldwin, A. Gelasco and V. Pecoraro, *Photosynth. Res.*, 1993, **38**, 303-308.
60. H. Zheng, Y. Zang, Y. Dong, V. G. Young and L. Que, *J. Am. Chem. Soc.*, 1999, **121**, 2226-2235.
61. A. Kütt, I. Leito, I. Kaljurand, L. Sooväli, V. M. Vlasov, L. M. Yagupolskii and I. A. Koppel, *J. Org. Chem.*, 2006, **71**, 2829-2838.
62. E. J. Larson, P. J. Riggs, J. E. Penner-Hahn and V. L. Pecoraro, *J. Chem. Soc., Chem. Commun.*, 1992, 102-103.
63. W. Kaim, A. Klein and M. Glöckle, *Acc. Chem. Res.*, 2000, **33**, 755-763.
64. M. Glöckle, W. Kaim, A. Klein, E. Roduner, G. Hübner, S. Zalis, J. van Slageren, F. Renz and P. Gütlich, *Inorg. Chem.*, 2001, **40**, 2256-2262.
65. N. G. Connelly and W. E. Geiger, *Chem. Rev.*, 1996, **96**, 877-910.
66. S. Friedrich, M. Schubart, L. H. Gade, I. J. Scowen, A. J. Edwards and M. McPartlin, *Chem. Ber./Recl.*, 1997, **130**, 1751-1759.
67. *SMART*, *Software Reference Manual*, Bruker AXS, Madison, WI, USA, 1998.
68. *SAINT*, *Software Reference Manual*, Bruker AXS, Madison, WI, USA, 1998.
69. G. M. Sheldrick, *SADABS, Program for empirical absorption correction of area detector data*, (2002), University of Göttingen, Germany.
70. G. M. Sheldrick, *SHELXTL Version 6.10 Reference Manual*, Bruker AXS Inc., Madison, Wisconsin, USA, 2000.
71. A. J. C. Wilson, ed., *International Tables for Crystallography*, First edn., Kluwer, Boston, 1995.